# An Investigation of the Thermal Stability of $Nd_xSc_yZr_{1-x-y}O_{2-\delta}$ Materials Proposed for Inert Matrix Fuel Applications

John R. Hayes, Andrew P. Grosvenor*
Department of Chemistry, University of Saskatchewan, Saskatoon, SK, Canada, S7N 5C9

Mouna Saoudi
Canadian Nuclear Laboratories Limited**, Chalk River, ON, Canada K0J 1J0

*Author to whom correspondence should be addressed
**Formerly, Atomic Energy of Canada Limited (AECL)

**Abstract**

Inert matrix fuels (IMF) consist of transuranic elements (i.e., Pu, Am, Np, Cm) embedded in a neutron transparent (inert) matrix, and can be used to "burn up" (transmute) these elements in current or Generation IV nuclear reactors. Yttria-stabilized zirconia has been extensively studied for IMF applications, but the low thermal conductivity of this material limits its usefulness. Other elements can be used to stabilize the cubic zirconia structure, and the thermal conductivity of the fuel can be increased through the use of a lighter stabilizing element. To this end, a series of $Nd_xSc_yZr_{1-x-y}O_{2-\delta}$ materials have been synthesized via a co-precipitation reaction and characterized by multiple techniques (Nd was used as a surrogate for Am). The long-range and local structures of these materials were studied using powder X-ray diffraction, scanning electron microscopy, and X-ray absorption spectroscopy. Additionally, the stability of these materials over a range of temperatures has been studied by annealing the materials at 1100 °C and 1400 °C. It was shown that the $Nd_xSc_yZr_{1-x-y}O_{2-\delta}$ materials maintained a single cubic phase upon annealing at high temperatures only when both Nd and Sc were present with $y \geq 0.10$ and $x+y > 0.15$.

*Keywords*: IMFs, nuclear fuel, X-ray absorption spectroscopy, K-edge, EXAFS, XANES

## 1. Introduction

Nuclear energy is used to produce electricity while producing minimal carbon emissions. [1,2] However, it produces radiotoxic waste that must be securely stored for thousands of years.[3–5] Transuranic elements (TRU; i.e., Pu, Am, Np, Cm) are largely responsible for the long-term radioactivity of spent nuclear fuel and the heat generated by these elements limits the storage capacity of geological facilities (e.g., Yucca Mountain).[4,6,7] The amount of transuranic species that must be stored can be reduced by incorporating them into nuclear fuels and "burning up" (transmuting) these elements in-reactor.[4,8–10] Inert matrix fuels, which consist of TRU species embedded in a neutron transparent (inert) material, have been proposed as nuclear fuels for use in Generation IV nuclear reactors.[8,11–14]

Cubic zirconia ($ZrO_2$), which adopts a fluorite-type structure, has been widely proposed for use as an inert matrix fuel due to its chemical durability, resistance to radiation damage, and high melting point (in addition to its low neutron absorption cross-section).[12,15–17] However, pure $ZrO_2$ in the cubic structure is only stable at temperatures above 2370 °C, it adopts a tetragonal structure at temperatures between 1170 °C and 2370 °C, and a monoclinic structure below 1170 °C.[18–21] The tetragonal and monoclinic structures are related to the cubic structure, and are connected to the cubic structure by shifts to lower symmetry arrangements as the temperature decreases.[22–25] Accompanying these phase transitions is a 3-5% increase in the volume and a significant drop in the thermal conductivity of the material.[19,26] An increase in the volume of the material is detrimental because fuel rods are engineered to precise specifications and expansion of the fuel pellet could lead to a fuel cladding failure.[27] A decrease in the thermal conductivity of the fuel material is also undesirable as this would lead to a greater fuel temperature which could lead to failure conditions.[27]

The cubic fluorite structure may be stabilized at room temperature by doping aliovalent cations into the system (i.e., $Y^{3+}$, $Sc^{3+}$).[12,20,22,28–30] The addition of an aliovaent cation introduces oxygen vacancies into the system, which, in addition to the size difference between the dopant cation and $Zr^{4+}$, act to stabilize the cubic structure [18,31]. Y-doped $ZrO_2$ materials have been extensively studied for use as an IMF material but these materials have a low thermal conductivity which leads to undesirable fuel pellet temperatures.[32–36] The thermal conductivity of the doped $ZrO_2$ materials could be increased if a lighter dopant element was used, as thermal conductivity increases as the molar mass of the material decreases.[37] Sc-doped $ZrO_2$ materials have been studied for use in solid-oxide

fuel cells (SOFC) due to their high oxygen conductivity. However, these materials have been shown to not be stable at SOFC operating temperatures, as the fluorite structure degrades. Studies have shown that the addition of a small amount (~1 wt%) of rare-earth element can enhance the stability of the fluorite structure at SOFC operating temperatures. Despite the interest in Sc-doped $ZrO_2$ materials as SOFC materials, very little research has been done to understand how the addition of significant amounts (>1 wt%) of an actinide will affect the structure of these materials.[29,38–40] To this end, a series of $Nd_xSc_yZr_{1-x-y}O_{2-\delta}$ materials have been synthesized and characterized. Nd has been used here as a surrogate for Am given its similar ionic radius and chemical reactivity.[20,41–43] The materials were made via a low-temperature co-precipitation method and the local and long-range structures of the compounds were studied by powder X-ray diffraction (XRD), scanning electron microscopy (SEM), and X-ray absorption spectroscopy (XAS). Additionally, given the wide range of temperatures that a fuel pellet will experience in a reactor, the stability of the fluorite structure adopted by these materials at high temperatures was also studied by annealing the as-synthesized materials at 1100 °C and 1400 °C. The annealed materials were then studied by powder XRD, SEM, and XAS as well. This study shows that both Nd and Sc are required to stabilize the fluorite structure of $Nd_xSc_yZr_{1-x-y}O_{2-\delta}$ materials, and changes in composition during both in-reactor and post-reactor service must be taken into account when considering these materials for IMF applications.

## 2. Experimental

### 2.1. Synthesis

The $Nd_xSc_yZr_{1-x-y}O_{2-\delta}$ materials were synthesized via a standard co-precipitation method.[44] Stoichiometric amounts of $Nd_2O_3$ (Alfa Aesar, 99.9%) and $Sc_2O_3$ (Alfa Aesar, 99.99%) were dissolved in boiling nitric acid while $ZrOCl_2 \cdot 8H_2O$ (Alfa Aesar, 99.9%) was dissolved in deionized water. The acidic Nd-Sc solution was then added to the aqueous $Zr^{4+}$ solution. Concentrated ammonia was added to the mixture, which resulted in the formation of a precipitate. The solid was collected via vacuum filtration and dried in air for 24 h. The dried precipitate was then calcined at 800 °C for 24 h in air, resulting in the final product. The thermal stability of the material was investigated by annealing ~0.07 g aliquots of the as-synthesized materials in air at 1100 °C and 1400 °C for 24 h. The bulk densities of the as-synthesized and annealed $Nd_xSc_yZr_{1-x-y}O_{2-\delta}$ materials were not measured.

The phase identification of the as-synthesized and annealed materials was performed using powder XRD. The powder XRD patterns were collected using a PANalytical Empyrean diffractometer using either Cu $K_{\alpha 1,2}$ ($\lambda$=1.5406 Å) or Co $K_{\alpha 1,2}$ ($\lambda$=1.7890 Å) radiation. Phase quantification was obtained by Rietveld refinement, which was performed using the PANalytical X'pert HighScore Plus software program.[45] Rietveld refinements were performed by fitting cubic $ZrO_2$, tetragonal $ZrO_2$, and monoclinic $ZrO_2$ phases to the data.[46–48] The phases used to model the diffraction data were adapted from the pure $ZrO_2$ patterns by adding Nd and Sc to the crystallographic site occupied by Zr. The site occupancies were set to be consistent with the ideal stoichiometry of each material. As an example, the cubic $ZrO_2$ pattern for the $Nd_{0.10}Sc_{0.10}Zr_{0.80}O_{1.90}$ pattern was generated by adding Sc and Nd to the Zr 4a site. The Zr site occupancy was set to 0.80 while the Sc and Nd site occupancies were each set to 0.10. The addition of Sc and Nd impacted the intensity of the modelled peaks and significantly improved the quality of the fit. For instance, in the example presented above when only Zr was used in the model the $R_{wp}$ was 11.82 while the $R_{wp}$ was 9.83 when Sc and Nd were also included in the model. The background was fitted using a 3rd order polynomial function which also included a 1/2θ term.

**2.2. Scanning Electron Microscopy**

SEM samples were prepared by pressing ~0.17 g of the as-synthesized material into a ¼" (0.635 cm) pellet before being sintered at 800 °C in air for 12 h. (The experimental configuration did not allow for measurement of the pellet press pressure or the pressing time.) The bulk densities of the pellets were not measured, and are likely much less than the theoretical density. Several of the pellets were subsequently annealed at 1400 °C for 24 h in air and air quenched. The pellets were embedded in a resin matrix and ground manually to a flat surface using SiC paper. The pellet surfaces were then polished using 0.25 μm diamond paste. The samples were coated with a thin carbon layer to reduce sample charging effects. A Zeiss Supra-55 WDS-VP SEM coupled with an Energy Dispersive X-ray Spectrometer (EDS) was used to collect SEM images and to carry out EDS mapping. The sample surface morphology was examined using secondary electron (SE) images. Samples were mapped by EDS for Zr, Sc, and Nd at 500x magnification, and the EDS maps were collected using an ~8 μm step size at an accelerating voltage of 20 kV. All EDS maps from a sample were collected at a the same spot.

### 2.3. X-ray Absorption Spectroscopy

#### 2.3.1. Zr K-edge, Nd $L_3$-edge XAS

Zr K-edge and Nd $L_3$-edge XAS spectra from the as-synthesized and annealed samples were collected using the CLS@APS Sector 20BM bending magnet beamline located at the Advanced Photon Source (APS), Argonne National Laboratory. A silicon (111) double crystal monochromator with a Rh harmonic rejection mirror was used, which has a resolution of 2.5 eV at 18000 eV (Zr K-edge) and 0.85 eV at 6000 eV (Nd $L_3$-edge). The beamline produces a photon flux of ~$10^{11}$ photons/s.[49] The samples were finely ground and sealed between layers of Kapton tape, and the number of layers was adjusted to maximize the absorption signal. In all cases, at least four layers were used, which resulted in a uniform sample thickness.

The Zr K-edge XAS spectra were collected in transmission mode using ion chambers filled with an 80% Ar:20% $N_2$ gas mixture. The spectra were calibrated using a Zr metal foil, having a known Zr K-edge absorption energy of 17998 eV, and the metal foil spectrum was measured in-line with the samples.[50] The X-ray absorption near-edge (XANES) region of the Zr K-edge spectra were measured using a 0.3 eV step through the absorption edge and the extended X-ray absorption fine structure (EXAFS) region of the Zr K-edge spectra was measured to k = 15 $Å^{-1}$ with a step size of 0.05 k.

The Nd $L_3$-edge XAS spectra were also collected in transmission mode. The intensity of the incident X-ray beam was measured using an ion chamber filled with a 70% He : 30% $N_2$ mixture and the transmitted beam intensity was measured using an ion chamber filled with $N_2$. The spectra were calibrated using a Mn foil (Mn K-edge = 6539 eV) which was measured separately.[50] The XANES region of the Nd $L_3$-edge spectra were collected using a 0.15 eV step through the edge. The EXAFS region was measured to k = 10.5 with a 0.05 k step size. (The Nd $L_3$-edge EXAFS range is limited by the Nd $L_2$-edge at 6722 eV.) All spectra were normalized and analyzed using the Demeter software suite.[51]

#### 2.3.2. Zr K-edge EXAFS Modelling

The EXAFS spectra were analyzed by fitting the parameters of the standard EXAFS equation:

$$\chi(k) = \sum_j \frac{N_j S_o^2}{kR_j^2} F_j(k) e^{-2\sigma_j^2 k^2} e^{-2R_j/\lambda} \sin\left(2kR_j + \phi_j(k)\right)$$

where $N_j$ is number of $j^{th}$ atoms at a distance $R_j$ from the absorbing atomic centre, $F_j(k)$ is the backscattering function, $\sigma_j^2$ is the Debye-Waller Factor, and $\phi_j(k)$ is the phase-shift function of the jth atom. These parameters are described in detail in previous publications.[52,53] Here, $N_j$ is equivalent to the coordination number (CN) and will be referred to as such. The Zr K-edge EXAFS spectra were analyzed by calculating $F_j(k)$, $\phi_j(k)$, and $\lambda$ for each set of scattering pairs in a given cluster using the FEFF6 code.[54] The other parameters were fit using a least-squares refinement as described below using the Artemis program, which is included in the Demeter software suite.[51]

A scattering cluster was generated based on a cubic zirconium structure using the parameter determined from the powder XRD patterns (*vide infra*). Two of the next-nearest-neighbor (NNN) Zr atoms were replaced by Nd and two of the NNN Zr atoms were replaced by Sc in the cluster when modelling the quaternary materials. It was necessary to add two of each dopant atoms into the system to generate the Zr–O–M scattering paths (M = Zr, Nd, Sc). (In the ternary materials only Sc or Nd was substituted into the system.) The $R_j$ and $\sigma^2$ parameters of the first shell Zr–O, second shell Zr–Zr, and third shell Zr–O (labelled as Zr–O2) paths were fitted as separate variables for each scattering path. The CN of each scattering path was initially set to reflect the stoichiometry of each phase and was then varied manually to improve the fit. The energy shift parameter, $\Delta E$, and $S_o^2$ were fitted across all scattering paths. The Zr–O–Zr, Zr–O–Sc, and Zr–O–Nd were also fitted using parameters from the single scattering paths. The changes in multi-scattering path lengths were modelled as $\Delta R_{Zr-O} + 0.5*\Delta R_{Zr-Zr/Sc/Nd}$, and the Debye-Waller factors were modelled as $\sigma^2_{Zr-O} + 0.5*\sigma^2_{Zr-Zr/Sc/Nd}$. The CNs of the multiscattering paths were changed to reflect the CNs of the Zr–Zr, Zr–Sc, and Zr–Nd single-scattering paths.

### 2.3.3. Sc K-edge, Zr $L_3$-edge XAS

Zr $L_3$-edge and Sc K-edge XANES spectra were collected using the Soft X-ray Microcharacterization Beamline (SXRMB, 06B1-01) located at the Canadian Light Source (CLS). The beamline has a photon flux of >1 x $10^{11}$ photons/s and provides a resolution of ~0.25 eV when using a Si (111) crystal monochromator.[55] Samples were mounted as fine powders spread on double-sided C tape. Both the Zr $L_3$-edge and Sc K-edge spectra were measured in total electron yield (TEY) mode using a 0.10 eV step through the absorption edge. The Zr $L_3$-edge spectra spectra were calibrated using Zr foil, which has a known Zr $L_3$-edge absorption energy of 2223 eV, and the Sc K-edge spectra were calibrated using Ti metal powder, having a known edge energy of 4966 eV.[50]

## 3. Results and Discussion

### 3.1. Powder XRD

Powder XRD patterns were collected from the as-synthesized and annealed $Nd_xSc_yZr_{1-x-y}O_{2-x}$ materials and are presented in Figures 1 and 2, and Figures S1 and S2 in the Supporting Information (SI). The diffraction patterns were analyzed using Rietveld refinement to determine the cubic unit cell parameter and phase composition of the materials. The results of this analysis are presented in Table 1 and Table S1. The peaks in the patterns from the as-synthesized materials heated at 800 °C are wider than those from the annealed samples. The wide peaks indicate the poor crystallinity of the as-synthesized materials and show that the as-synthesized materials are significantly less crystalline than the materials annealed at higher temperatures.[56] This is consistent with the synthetic conditions as higher annealing temperatures should lead to a more crystalline and ordered material.

Only peaks associated with the cubic fluorite phase were observed in the patterns from the as-synthesized materials. However, the cubic phase was not stable when the ternary phases were annealed at high temperature. The tetragonal phase was formed in the ternary $Nd_{0.25}Zr_{0.75}O_{1.88}$ compound when it was annealed at 1100 °C and the Rietveld analysis indicated that the material was ~33% tetragonal and 67% cubic phase (see Table 1). Both the tetragonal and monoclinic phases were observed when $Nd_{0.25}Zr_{0.75}O_{1.88}$ was annealed at 1400 °C, resulting in a multi-phase material containing 30.9% monoclinic phase, 3.5% tetragonal phase, and 64.7% cubic phase. An ordered Sc-Zr-O β-phase was formed when $Sc_{0.25}Zr_{0.75}O_{1.88}$ was annealed at 1400 °C. The structure of this β-phase material is complex and poorly understood, though it can be described as a superstructure of the fluorite structure in which the O-vacancies are ordered.[39,40,57–60] The formation of a rhombahedral β-phase Sc-Zr-O observed in this study is consistent with previous studies of Sc-substituted zirconia, in which rhombahedral Sc-Zr-O phases were observed when Sc-$ZrO_2$ materials were heated at temperatures >600 °C.[39,40,57–60]

The stability of the cubic fluorite structure adopted by the quaternary $Nd_xSc_yZr_{1-x-y}O_{2-\delta}$ materials was found to vary with composition. A phase change was observed in the $Nd_{0.20}Sc_{0.05}Zr_{0.75}O_{1.88}$ material when it was annealed at high temperature. The cubic structure decomposed into a mix of tetragonal and cubic phase when this composition was annealed at 1100 °C. Only a small (8.8%) amount of monoclinic phase was observed when $Nd_{0.20}Sc_{0.05}Zr_{0.75}O_{1.88}$ was annealed at 1400 °C (Table 1). Monoclinic zirconia was also observed when

$Nd_{0.15}Sc_{0.05}Zr_{0.80}O_{1.90}$ was annealed at 1400 °C (Table S1, Figure S2a). These results indicate that a minimum amount of Sc ($y \geq 0.10$) must be doped into the system to stabilize the cubic phase in the quaternary materials. In addition, neither the $Nd_{0.10}Sc_{0.05}Zr_{0.85}O_{1.92}$ nor the $Nd_{0.05}Sc_{0.10}Zr_{0.85}O_{1.92}$ materials were stable upon annealing at high temperatures. These results indicate that the amount of dopant added to the material (i.e., x+y) must be greater than 0.15 to stabilize the cubic zirconia phase at a wide range of temperatures. No phase changes were observed when the $Nd_xSc_yZr_{1-x-y}O_{2-\delta}$ materials with $x+y > 0.15$ and $y \geq 0.10$ were annealed at temperatures up to 1400 °C (see Table 1, Table S1).

The cubic unit cell parameters are plotted in Figure S3 in the SI as a function of composition. The changes in the unit cell with composition deviated from the values expected from Vegard's law (i.e., the change was not linear) and the unit cells of the end member as-synthesized $Nd_{0.25}Zr_{0.75}O_{1.88}$ and $Sc_{0.25}Zr_{0.75}O_{1.88}$ materials were much larger than expected.[61] This is in contrast to the $Nd_xY_yZr_{1-x-y}O_{2-\delta}$ system, where the lattice parameter varied according to Vegard's law.[53] This could be indicative of more disorder in these compounds when compared to the quaternary materials. The unit cell of the materials expanded slightly upon annealing with the exception of $Nd_{0.20}Sc_{0.05}Zr_{0.75}O_{1.88}$, which contracted slightly. This expansion varied between 0.0028-0.0365 Å and the magnitude of the change generally decreased as the Sc replaced Nd in the system. Again, the unit cells of the end-member $Nd_{0.25}Zr_{0.75}O_{1.88}$ and $Sc_{0.25}Zr_{0.75}O_{1.88}$ materials deviated from Vegard's Law. This deviation in the annealed materials may be explained by the large changes in phase composition that occurred upon annealing (*vide supra*).

### 3.2. SEM and EDS

The as-synthesized and annealed materials were characterized by SEM. Representative secondary electron (SE) micrographs are presented in Figure 3 and Figure S4 in the SI. The micrographs from the as-synthesized pellets (Figure 3a-d) showed that the surfaces contained large, faceted grains. The surface morphology did not appear to depend on composition. The surfaces became porous upon annealing at 1400 °C and no faceted surfaces were observed. The surfaces of the annealed pellets were consistent with the surfaces of previously studied $Nd_xY_yZr_{1-x-y}O_{2-\delta}$ materials that were synthesized via a high temperature solid-state route [53].

This indicates that surface morphology is strongly dependent on annealing temperature but independent of composition.

Energy dispersive spectroscopy (EDS) elemental maps were also collected from the materials and these are presented in Figures 4-6 and Figures S5-7 in the SI. In general, lighter shaded regions indicate regions of higher elemental concentration while darker regions indicate areas of lower elemental concentration. However, some shadowing can be seen due to topography of the polished pellet surface. This shadowing is most prevalent in Figure 6, which shows Zr $L_\alpha$ maps from the $Nd_xSc_yZr_{1-x-y}O_{2-\delta}$ samples. The dark regions in these EDS maps correspond well to dark regions found in Sc and Nd EDS maps from the same composition, further confirming that the low intensity regions are due to shadowing effects, and not changes in concentration. (All of the EDS maps and SEM images were collected from a single spot and magnification for each individual sample.) Figure 4 shows the Nd $L_\alpha$-maps of several as-synthesized materials (Figures 4a-c) and materials annealed at 1400 °C (Figures 4d,e). No aggregation was observed in the Nd $L_\alpha$-map from the $Nd_{0.05}Sc_{0.05}Zr_{0.75}O_{1.88}$ sample annealed at 1400 °C due to the poor signal-to-noise ratio of the map (Figure 4f). Nd is relatively evenly distributed in the as-synthesized materials, though some spots where higher Nd concentrations were observed (Figure 4a-c). In contrast, the Nd distribution becomes heterogeneous upon annealing the materials at 1400 °C, and distinct Nd aggregates were observed within the materials (Figure 4d,e). The observed changes in the Nd EDS maps are distinct, and the Nd distributions are qualitatively different between the as-synthesized and annealed samples. The nature of these changes indicates that the Nd distribution shifts, and that these results are not a product of changes in the surface shadowing. This change in Nd distribution upon high-temperature annealing was observed in all materials studied, and suggests that Nd segregation is a thermodynamically favorable process, rather than a kinetically driven process as was previously postulated for $Nd_xY_yZr_{1-x-y}O_{2-\delta}$ materials made via a solid-state reaction method.[53] The formation of Nd aggregates is generally negative when considering these materials for IMF applications as the formation of areas of high actinide concentration in an IMF would lead to uneven heat distribution and activity throughout the fuel pellet.[27]

The Sc $K_\alpha$ and Zr $L_\alpha$ maps are presented in Figures 5 and 6, respectively. A small number of Sc bright spots were observed in the as-synthesized materials, but these appeared to disperse upon annealing at 1400 °C. In general, it was observed that both Zr and Sc were dispersed homogenously throughout these materials. The

distribution of both elements remained generally homogenous after high-temperature annealing as well. This indicates that both Zr and Sc do not segregate in the materials upon annealing.

### 3.3. Zr K-edge

#### 3.3.1. XANES

Zr K-edge XANES spectra were collected from the as-synthesized and high-temperature annealed $Nd_xSc_yZr_{1-x-y}O_{2-\delta}$ materials and these spectra are presented in Figure 7 and Figures S8 and S9 in the SI. Three features are observed in these spectra, labelled as A, B, and C in Figure 7a. Feature A is known as the pre-edge and is due to forbidden, quadrupolar Zr 1s → 4d excitations.[62,63] Features B and C constitute the main-edge, which is comprised of dipolar Zr 1s → 5p excitations.[62,63] The intensity and shape of the pre-edge depends on the geometry of the coordination environment around the Zr metal centre.[64] The pre-edge does not change with composition, which indicates the symmetry of the Zr coordination environment likely does not vary with changing composition.

Small changes in the main-edge were observed to occur as the composition of the as-synthesized materials was varied. Feature B moved to higher energy and the intensity of features B and C increased as Sc replaced Nd in the system. A comparison to previously collected Zr K-edge spectra from tetragonal and monoclinic $ZrO_2$ systems indicates that these changes were due to a change in the symmetry of the Zr-bearing phases.[53] Therefore, it is concluded from these changes in the Zr K-edge XANES spectra that the symmetry of the local Zr coordination environment of the $Nd_xSc_yZr_{1-x-y}O_{2-\delta}$ materials decreased slightly as Sc replaces Nd in these materials.

The spectrum from the $Nd_{0.25}Zr_{0.75}O_{1.88}$ material changes upon annealing with the intensity of the main-edge at ~18020 eV increasing and feature B shifting to slightly higher energy (Figure 7b). This change is consistent with the formation of a lower symmetry $ZrO_2$ phase, which is consistent with the powder XRD results.[53] The spectra from the other $Nd_xSc_yZr_{1-x-y}O_{2-\delta}$ materials do not change upon high-temperature annealing. This result is somewhat surprising as the powder XRD results indicated that β-phase Sc-Zr-O formed when $Sc_{0.25}Zr_{0.75}O_{1.88}$ was annealed at 1400 °C. However, the β-phase Sc-Zr-O is a derivative of the fluorite supercell and the main difference between the fluorite structure and the structure of the β-phase Sc-Zr-O material is the ordering of anion vacancies within the system.[39,40,57–60] The Zr coordination environment remains largely

unchanged in these materials, and it is expected that any changes between the spectra from the cubic phase and β-phase would be too small to be observed given the relatively low energy resolution of the Zr K-edge spectra. In general, the Zr K-edge XANES spectra show that the local environment around Zr did not change significantly upon high-temperature annealing when Sc was present in the material.

### 3.3.2. EXAFS

The EXAFS region of the Zr K-edge XAS spectra were collected from the as-synthesized and annealed $Nd_xSc_yZr_{1-x-y}O_{2-\delta}$ materials and the Fourier transformed spectra are presented in Figure 8 and Figures S10-12 in the SI. Three peaks were observed in these spectra, and these are labelled as D, E, and E' in Figure 8a. Peak D is associated with the nearest-neighbor (NN) Zr–O scattering path and peak E is associated with the next-nearest-neighbor (NNN) Zr–Zr, Zr–Sc, and Zr–Nd scattering paths. Peak E' is primarily attributed to a shoulder of the Zr–Sc single-scattering path. The intensity of Peak E was mostly independent of composition, though a small decrease in intensity was observed when Nd was added to the system. It is likely that this change was due to interference between the Zr–Zr, Zr–Sc, and Zr–Nd paths, and does not represent a physical change. The intensity of Peak E' increased with increasing Sc content. This change with increasing Sc content can be explained by the increased number of Sc NNN atoms as this peak is directly related to the Zr–Sc scattering path.

The intensity of peak D increased as Sc replaced Nd in the system. This change may indicate that the Zr coordination number increases with increasing Sc content. It has been previously shown that O-vacancies are preferentially located around Nd in Nd-$ZrO_2$ systems while O-vacancies are preferentially located around the Sc metal centres in Sc-$ZrO_2$ systems.[17,65,66] Here, the O-vacancies are likely pulled away from the Zr metal centres as Sc is introduced in the system resulting in an increase in the Zr CN. This phenomenon has been previously ascribed to size effects and differences in Sc-vacancy binding energy compared to the Zr-vacancy binding energy in $R_2O_3$-$ZrO_2$ (R = rare-earth, Y, Sc) systems, and the results here serve to further confirm these prior studies.[17,65,66]

The Fourier transformed EXAFS spectra from the as-synthesized and annealed materials are compared in Figures 8b and Figures S9-S11 in the SI. The intensities of peaks D, E, and E' increased with increasing annealing temperature with the exception of the $Nd_{0.10}Sc_{0.05}Zr_{0.85}O_{1.92}$ and $Nd_{0.05}Sc_{0.10}ZrO_{1.92}$ samples (Figure S9a, c). In the case of these materials, phase changes were also observed via powder XRD (Figure S2), and, in general, these

materials behaved differently than the other $Nd_xSc_yZr_{1-x-y}O_{2-\delta}$ materials. Here, the discussion about these materials is limited to concluding that $Nd_xSc_yZr_{1-x-y}O_{2-\delta}$ compounds with $x+y \leq 0.15$ are not stable under high-temperature annealing conditions and are therefore unsuitable for IMF applications.

With regards to the $Nd_xSc_yZr_{1-x-y}O_{2-\delta}$ compounds with $x+y > 0.15$, the increased intensity of the peaks can largely be attributed to an increase in the ordering of the local and long-range structures in these materials upon high-temperature annealing. This conclusion is consistent with the powder XRD results, as the diffraction peaks were observed to become more narrow upon annealing (*vide supra*). However, the increase in the intensity of feature D upon annealing was not consistent between material compositions, and the intensity appears to increase more when the Sc loading is high. This may indicate that the Zr CN is also increasing in these cases in addition to the increased ordering. This could be caused by a migration of O-vacancies to sites adjacent to the Sc metal centres (*vide infra*). These comparisons indicate that the $Nd_xSc_yZr_{1-x-y}O_{2-\delta}$ materials made at 800 °C become more ordered upon high-temperature annealing when $x+y > 0.15$.

The EXAFS spectra were also modelled and the resulting fits are plotted along with the Zr K-edge spectra in Figures 8c,d and Figures S13-23 in the SI. The parameters of these fits are enumerated in Table 2 and Table S2 in the SI. Overall, there is a good agreement between the data and the modelled spectra, and the R-factors of the models are indicative of quality fits (see Table 2). The Zr–O bond distance was found to be ~2.15 Å in all cases and the Zr–Zr bond distance was found to vary between 3.53-3.58 Å, although the differences in the Zr–Zr bond distances were not statistically significant. Both the Zr–O and Zr–Zr distances are in agreement with previously reported values for $Nd_xY_yZr_{1-x-y}O_{2-\delta}$ systems.[53] The Zr–Sc bond distances and Zr–Nd scattering distances determined from the as-synthesized and annealed $Sc_{0.25}Zr_{0.75}O_{1.88}$ and as-synthesized $Nd_{0.15}Sc_{0.10}Zr_{0.75}O_{1.88}$ were all within a statistically similar range. However, the Zr–Nd bond distance in $Nd_{0.15}Sc_{0.10}Zr_{0.75}O_{1.88}$ was observed to decrease to 3.36(3) Å when the material was annealed at 1400 °C. A similar phenomenon was observed when quaternary $Nd_xY_yZr_{1-x-y}O_{2-\delta}$ compounds were annealed at 1400 °C.[53] In this previous study, the short Zr–Nd bond lengths, which are not expected in a fluorite structure, were proposed to arise from the *possible* formation of a c-$Nd_2O_3$ structure.[53] It also appears that a c-$Nd_2O_3$ type-material *could* be forming in the $Nd_xSc_yZr_{1-x-y}O_{2-\delta}$ compounds annealed at high temperatures, though it is also possible that this determined short bond distance was

a result of an error in the model fitted to the data. In general, further research must be performed to determine if a c-$Nd_2O_3$ phase could be present in these materials.

The $\sigma^2$ values of each scattering path did not change with composition or annealing temperature. The $\sigma^2$ values were all physically plausible values with the exception of the $\sigma^2$ values of the Zr–Sc and Zr–Nd scattering paths from $Nd_{0.15}Sc_{0.10}Zr_{0.75}O_{1.88}$. In the case of this material, the $\sigma^2$ values of 0.005 and 0.004 were smaller than what would be expected for a NNN bond length. The Zr–Sc and Zr–Nd coordination numbers also had to be changed when fitting the spectrum from the $Nd_{0.15}Sc_{0.10}Zr_{0.75}O_{1.88}$ material annealed at 1400 °C to prevent $\sigma^2$ for these scattering paths from being negative. These low $\sigma^2$ values may indicate that some segregation of Nd, Sc, and Zr occurs in the materials after annealing at high temperature. This explanation is consistent with the SEM and EDS results as well, which showed that the Nd distribution became heterogeneous after annealing at 1400 °C. To summarize, the Zr K-edge EXAFS results show that the Zr coordination number changes with composition and upon annealing. The results also show that the distribution of Zr, Sc, and Nd in the material also likely changes when Nd is added to the Sc-$ZrO_2$ system and upon annealing.

### 3.4. Zr $L_3$-edge

Zr $L_3$-edge spectra were collected from several of the as-synthesized and annealed $Nd_xSc_yZr_{1-x-y}O_{2-\delta}$ compounds, and are presented in Figure 9 and Figure S24 in the SI. Two peaks, labelled as F and G in Figure 9a, were observed in these spectra due to crystal field splitting of the Zr 4d states. Peak F is attributed to Zr 2p → 4d $e_g$ transitions while peak G arises from Zr 2p → 4d $t_{2g}^*$ excitations. Peak G was observed to slightly increase as Sc replaced Nd in the system, which may indicate that the coordination environment around Zr became more symmetric. This is consistent with a shift to a tetragonal phase, in which the coordination environment is more symmetric and the Zr CN is 8, and these results agree with the Zr K-edge XANES results (*vide supra*). However, this change is small, and only represents a minor shift in the coordination environment, which is likely why changes were not observed in the pre-edge of the Zr K-edge XANES spectra.

The Zr $L_3$-edge spectra did not change significantly upon high-temperature annealing of the materials (Figure 9b). With the exception of the spectra from the $Nd_{0.15}Sc_{0.05}Zr_{0.80}O_{1.90}$ sample, the changes were small and not significant. The spectrum from the $Nd_{0.15}Sc_{0.05}Zr_{0.80}O_{1.90}$ sample did change significantly as the intensity of feature G decreased and there was a slight increase in the intensity of the spectrum at ~2226 eV when the material

was annealed at 1400 °C. A comparison of the spectra from the $Nd_xSc_xZr_{1-x-y}O_{2-\delta}$ materials to the spectrum from monoclinic $ZrO_2$ (Figure 9a) indicates that this change is likely due to the formation of monoclinic zirconia upon annealing. The powder XRD results from this sample also indicated that monoclinic zirconia was formed upon annealing (see Figure S2). Overall, these results further indicate that the coordination environment around Zr in $Nd_xSc_yZr_{1-x-y}O_{2-\delta}$ materials does not change significantly when annealed at temperatures up to 1400 °C.

### 3.5. Sc K-edge

The Sc K-edge XANES spectra from several of the as-synthesized and high temperature annealed $Nd_xSc_yZr_{1-x-y}O_{2-\delta}$ materials are presented in Figure 10. The spectra exhibit three pre-edge peaks, labelled as $H_1$, $H_2$, and $H_3$ in Figure 10a, which result from Sc 1s → 3d transitions. Two main-edge peaks, labelled as $I_1$ and $I_2$, were also observed, and arise from Sc 1s → 4p transitions. Beyond this, a definitive and detailed assignment of each peak is not possible as there is relatively little literature available regarding analysis of the Sc K-edge.[67–70] However, there is a similarity in shape between the Sc K-edge spectra and Ti K-edge spectra from defect fluorite and pyrochlore type systems.[71,72] Given the close proximity of Sc and Ti on the periodic table, it seems reasonable to assume that the features in the Sc K- and Ti K-edge spectra would also have similar origins. Based on this, the details of the peak origins can be tentatively assigned and further analyzed. Feature $H_1$ likely arises from Sc 1s → 3d $e_g$ transitions and feature $H_2$ is likely due to Sc 1s → 3d $t_{2g}^*$ excitations. Feature $H_3$ is likely due to an excitation known as an intersite hybrid feature, in which Sc 1s electrons are excited to non-local states consisting of absorbing atom 4p states interacting with next-nearest-neighbor d-states through O 2p states. Continuing the analogy to the Ti K-edge, feature $I_1$ is assigned to excitations of the 1s electrons to Sc 4p states interacting with O 2p states while feature $I_2$ can simply be assigned to transitions to empty Sc 4p states.

The line shape of the main-edge of the Sc K-edge spectra from the $Nd_xSc_yZr_{1-x-y}O_{2-\delta}$ is similar to that of the spectrum from $[Sc(OH_2)_8](CF_3SO_3)_3$, in which Sc occupies a symmetric 8-fold coordination environment.[68] The Sc K-edge spectra also bear a close resemblance to Sc-doped $CeO_2$ materials, which adopt a fluorite structure.[69] These similarities likely indicate that Sc occupies a cubic coordination site. The weak intensities of the pre-edge features indicate there is minimal Sc 4p-Sc 3d mixing and that the Sc coordination environment likely contains an inversion centre, which further supports the conclusion that Sc occupies a cubic coordination site.

Only slight changes in the spectra from the $Nd_xSc_yZr_{1-x-y}O_{2-\delta}$ materials were observed when the composition was varied (Figure 10a) and when the materials were annealed at high temperature (Figure 10b). These results indicate that only minor changes in the local Sc coordination environment occurred when the composition was varied and when the materials were annealed at high temperature.

### 3.6. Nd $L_3$-edge

Nd $L_3$-edge XANES spectra were collected from the as-synthesized and annealed $Nd_xSc_yZr_{1-x-y}O_{2-\delta}$ materials, and these spectra are presented in Figure 11. A single, intense peak is observed in these spectra and this peak is attributed to Nd 2p → Nd 5d transitions.[73] Figure 11a shows that as the Nd content in the materials increased there was a small decrease in the intensity of the white line. This decrease is likely due to changes in the electronegativity of the NNN atoms. The average electronegativity of the NNN atom decreases as Nd ($\chi = 1.07$) replaces Sc ($\chi = 1.20$).[74] The reduced electronegativity results in less electron density being pulled away from the absorbing Nd atom, and slightly reduces the number of unoccupied states that the core electron can be excited to. This reduction would result in the reduced peak intensity observed here.

The spectra from the as-synthesized and high-temperature annealed $Nd_xSc_yZr_{1-x-y}O_{2-\delta}$ compounds are compared in Figure 11b. The spectra from the as-synthesized and annealed compounds are similar, indicating that only minimal changes in the structure around Nd occur upon annealing. The broad peak at ~6250 eV slightly increased with annealing temperature. This peak is attributed to multi-scattering resonances, in which the excited photoelectron scatters off multiple neighboring atoms. The increased intensity of this peak indicates that the local structures around Nd became more ordered upon annealing, which is also consistent with the powder XRD results (*vide supra*). Overall, the Nd $L_3$-edge spectra indicate that the Nd coordination environment in $Nd_xSc_yZr_{1-x-y}O_{2-\delta}$ does not change upon thermal treatment.

### 3.7. Mechanistic Insights

The EDS results provide insight into the mechanism of how Sc acts to stabilize the fluorite structure in the $Nd_xSc_yZr_{1-x-y}O_{2-\delta}$ materials. The EDS images showed that when all of the materials were annealed at 1400 °C the Nd became segregated within the material. This segregation led to areas where the Nd content is too low to stabilize the fluorite structure in $Nd_xZr_{1-x}O_{2-\delta}$ materials, resulting in the formation of lower symmetry monoclinic

and tetragonal phases. The Zr coordination number in monoclinic $ZrO_2$ is reduced to 7 as the structure distorts to this lower symmetry phase. Therefore, it is not expected that this segregation would result in an increase in the Zr CN despite the increased O-content in monoclinic $ZrO_2$ compared to O-deficient $Nd_xZr_{1-x}O_{2-\delta}$. The effects of the Nd segregation were mitigated by the addition of Sc into the system, which did not segregate upon annealing and kept the concentration of 3+ cations throughout the annealed material at level high enough to stabilize the fluorite structure. This stabilization mechanism has been previously shown to occur in $Nd_xY_yZr_{1-x-y}O_{2-\delta}$ systems, where Y acts in a similar manner to stabilize the fluorite structure.[53]

The mechanism by which Nd acts to prevent the formation of the β-phase Sc-Zr-O in the $Nd_xSc_yZr_{1-x-y}O_{2-\delta}$ is more complex, though the XAS results provide insights into this phenomenon. The β-phase Sc-Zr-O forms when the anion vacancies become ordered, forming a fluorite superstructure. The fluorite structure of the as-synthesized $Sc_yZr_{1-y}O_{2-\delta}$ materials was a metastable state formed via the low-temperature co-precipitation method. In this case, high disorder within the system prevents the formation of the highly ordered β-phase. The Zr K-edge EXAFS spectra showed that the Zr CN increased upon annealing, which is consistent with a shift in O-vacancies away from Zr. The Zr K-edge XAS results also showed that the change in CN upon annealing decreased as Nd replaced Sc in the $Nd_xSc_yZr_{1-x-y}O_{2-\delta}$ compounds. These results show that the O-vacancies migrated to more ordered positions upon annealing. The Nd prevented the migration of O-vacancies within the material, which prevented the formation of β-phase Sc-Zr-O. This is consistent with several other studies of RE-doped Sc-$ZrO_2$ systems which showed that the anion mobility decreased as the dopant cation size increased.[75–77] From these results it can be concluded that Sc-doped zirconia is not appropriate for IMF applications.

**4. Conclusions**

The thermal stability and local and long-range structures in a series of $Nd_xSc_yZr_{1-x-y}O_{2-\delta}$ materials have been characterized using a number of techniques. The powder XRD results showed that neither the $Nd_xZr_{1-x}O_{2-\delta}$ nor the $Sc_yZr_{1-y}O_{2-\delta}$ materials were stable when annealed at $T \geq 1100$ °C. This indicates that the ternary materials are not suitable for IMF applications. The addition of a small amount of Sc to the system ($y = 0.05$) greatly reduced the amount of monoclinic and tetragonal $ZrO_2$ that was formed upon annealing while the addition of slightly more Sc ($y = 0.10$) completely stabilized the cubic structure. The fluorite structure was only stable at high

temperatures when x+y > 0.15. The EDS data indicates that Sc stabilizes the cubic structure by maintaining a sufficient concentration of 3+ cations in the system when Nd segregates in the materials upon annealing. The fluorite structure of the $Sc_yZr_{1-y}O_{2-\delta}$ materials was also not stable at high temperatures, and a β-phase Sc-Zr-O oxide was formed when these materials were annealed. However, the addition of Nd to the system prevented this transformation. The XANES results indicated that the local coordination environments around the Sc and Nd metal centres were mostly independent of changes in composition and thermal treatment. This indicates that the local structures in $Nd_xSc_yZr_{1-x-y}O_{2-\delta}$ materials with x+y > 0.15 are stable at high temperatures. The Zr K-edge EXAFS results indicated that the Zr CN decreased as Nd replaced Sc in the materials and that changes in the Zr CN decreased with increasing Nd content upon annealing.

A mechanism by which the fluorite structure is stabilized in the quaternary $Nd_xSc_yZr_{1-x-y}O_{2-\delta}$ materials was proposed from these results. The addition of Sc limits the effect of Nd migration upon annealing, likely by ensuring that an adequate number of O-vacancies remain in the fluorite system. This results in the stabilization of the fluorite structure upon high-temperature annealing. Conversely, the addition of Nd prevents the formation of an ordered β-phase by limiting O-vacancy migration within the fluorite phase. The results presented here indicate that both Nd and Sc are required to stabilize the fluorite structure in $Nd_xSc_yZr_{1-x-y}O_{2-\delta}$ materials at temperatures up to 1400 °C.

**Acknowledgements**

The Natural Sciences and Engineering Research Council (NSERC) of Canada supported this work through a discovery grant awarded to APG. JRH would also like to thank NSERC for financial support through the Canada Graduate Scholarship program and the University of Saskatchewan. The Canadian Foundation for Innovation (CFI) is thanked for providing funds to purchase the PANalytical Empyrean powder X-ray diffractometer used in this work. The authors extend their thanks to Dr. Zou Finfrock and Dr. Robert Gordon for their help in carrying out XAS measurements at 20BM (CLS@APS Sector 20, APS), and Ms. Aimee Maclennan and Dr. Youngfeng Hu for help in carrying out the XANES measurements on the SXRMB beamline (06B1-1, CLS). In addition, Mr. M. R. Ruffadin and Ms. E. Aluri (Department of Chemistry, University of Saskatchewan) are thanked for helping with the collection of the XANES spectra presented in this study. The authors would like

to thank Dr. R. Ham-Su and Dr. L. Dickson of the Canadian Nuclear Laboratories Limited (CNL) for support of this work. Mr. J. Mouris and Mr. C. Mayhew (CNL) are thanked for their help in the sample preparation for SEM and for collecting the SEM images and EDS measurements. Access to Sector 20 was obtained through the CLS-APS Partnership Agreement. Sector 20 facilities at the Advanced Photon Source, and research at these facilities, are supported by the US Department of Energy - Basic Energy Sciences, the Canadian Light Source and its funding partners, the University of Washington, and the Advanced Photon Source. Use of the Advanced Photon Source, an Office of Science User Facility operated for the U.S. Department of Energy (DOE) Office of Science by Argonne National Laboratory, was supported by the U.S. DOE under Contract No. DE-AC02-06CH11357. The CLS is supported by NSERC, the National Research Council of Canada, the Canadian Institutes of Health Research, the Province of Saskatchewan, Western Economic Diversification Canada, and the University of Saskatchewan.

**Supporting Information Available**: The supporting information includes additional powder XRD patterns and fits of the XAS spectra from the $Nd_xSc_yZr_{1-x-y}O_{2-\delta}$ compounds.

**Author Information**: E-mail: andrew.grosvenor@usask.ca, Phone: (306) 966-4660, Fax: (306) 966-4730

**References**


(1) Hoffert, M. I.; Caldeira, K.; Benford, G.; Criswell, D. R.; Green, C.; Herzog, H.; Jain, A. K.; Kheshgi, H. S.; Lackner, K. S.; Lewis, J. S.; Lightfoot, H. D.; Manheimer, W.; Mankins, J. C.; Mauel, M. E.; Perkins, L. J.; Schlesinger, M. E.; Volk, T.; Wigley, T. M. L. *Science* **2002**, *298*, 981–987.

(2) Kharecha, P. A.; Hansen, J. E. *Environ. Sci. Technol.* **2013**, *47*, 4889–4895.

(3) Rempe, N. T. *Prog. Nucl. Energy* **2007**, *49*, 365–374.

(4) Prítrský, J.; Nečas, V. *Prog. Nucl. Energy* **2012**, *54*, 36–40.

(5) Long, J. C. S.; Ewing, R. C. *Annu. Rev. Earth Planet. Sci.* **2004**, *32*, 363–401.

(6) Salvatores, M.; Palmiotti, G. *Prog. Part. Nucl. Phys.* **2011**, *66*, 144–166.

(7) Lombardi, C.; Luzzi, L.; Padovani, E.; Vettraino, F. *Prog. Nucl. Energy* **2008**, *50*, 944–953.

(8) Ledergerber, G.; Degueldre, C.; Heimgartner, P.; Pouchon, M. A.; Kasemeyer, U. *Prog. Nucl. Energy* **2001**, *38*, 301–308.

(9) Lombardi, C.; Mazzola, A. *Ann. Nucl. Energy* **1996**, *23*, 1117–1126.

(10) Pöml, P.; Konings, R. J. M.; Somers, J.; Wiss, T.; de Haas, G. J. L. M.; Klaassen, F. C. In *Comprehensive Nuclear Materials Volume 3*; Konings, R. J. M., Allen, T. R., Stoller, R. E., Yamanaka, S., Eds.; Elsevier, 2012; pp 237–256.

(11) Ronchi, C.; Ottaviani, J. P.; Degueldre, C.; Calabrese, R. *J. Nucl. Mater.* **2003**, *320*, 54–65.

(12) Degueldre, C. *J. Alloys Compd.* **2007**, *444-445*, 36–41.

(13) Degueldre, C.; Paratte, J. M. *J. Nucl. Mater.* **1999**, *274*, 1–6.

(14) Yu, T.; Wu, X.; Xie, J.; Qin, M.; Li, Z.; Liu, Z.; Chen, H. *Prog. Nucl. Energy* **2015**, *78*, 341–345.

(15) Momma, K.; Izumi, F. *J. Appl. Crystallogr.* **2008**, *41*, 653–658.

(16) Lumpkin, G. R. *Elements* **2006**, *2*, 365–372.

(17) Zacate, M. O.; Minervini, L.; Bradfield, D. J.; Grimes, R. W.; Sickafus, K. E. *Solid State Ionics* **2000**, *128*, 243–254.

(18) Shibata, N.; Katamura, J.; Kuwabara, A.; Ikuhara, Y.; Sakuma, T. *Mater. Sci. Eng. A* **2001**, *312*, 90–98.

(19) Guo, X. *Phys. Status Solidi* **2000**, *177*, 191–201.

(20) Lemonnier, S.; Grandjean, S.; Robisson, A.-C.; Jolivet, J.-P. *Dalton Trans.* **2010**, *39*, 2254–2262.

(21) Kinoshita, H.; Kuramoto, K.; Uno, M.; Yanagi, T.; Yamanaka, S.; Mitamura, H.; Banba, T. *J. Am. Ceram. Soc.* **2000**, *83*, 391–396.

(22) Li, P.; Chen, I.; Penner-Hahn, J. E. *Phys. Rev. B* **1993**, *48*, 63–73.

(23) Belin, R. C.; Martin, P. M.; Valenza, P. J.; Scheinost, A. C. *Inorg. Chem.* **2009**, *48*, 5376–5381.

(24) Xu, G.; Ming, W.; Yao, Y.; Dai, X.; Zhang, S.-C.; Fang, Z. *Eur. Lett.* **2008**, *82*, 67002.

(25) Zhang, F.; Chupas, P. J.; Lui, S. L. A.; Hanson, J. C.; Caliebe, W. A.; Lee, P. L.; Chan, S.-W. *Chem. Mater.* **2007**, *19*, 3118–3126.

(26) Bocanegra-Bernal, M. H.; Díaz de la Torre, S. *J. Mater. Sci.* **2002**, *37*, 4947–4971.

(27) Olander, D. *J. Nucl. Mater.* **2009**, *389*, 1–22.

(28) Wang, C.; Zinkevich, M.; Aldinger, F. *Pure Appl. Chem.* **2007**, *79*, 1731–1753.

(29) Huang, H.; Hsieh, C.-H.; Kim, N.; Stebbins, J.; Prinz, F. *Solid State Ionics* **2008**, *179*, 1442–1445.

(30) Badwal, S. P. S.; Ciacchi, F. T.; Milosevic, D. *Solid State Ionics* **2000**, *136-137*, 91–99.

(31) Zavodinsky, V. G.; Chibisov, A. N. *Phys. Solid State* **2006**, *48*, 363–368.

(32) Kamel, N.; Aït-Amar, H.; Taouinet, M.; Benazzouz, C.; Kamel, Z.; Fodil-Cherif, H.; Telmoune, S.; Slimani, R.; Zahri, A.; Sahel, D. *Prog. Nucl. Energy* **2006**, *48*, 70–84.

(33) Degueldre, C.; Hellwig, C. *J. Nucl. Mater.* **2003**, *320*, 96–105.

(34) Pouchon, M. A.; Degueldre, C.; Tissot, P. *Thermochim. Acta* **1998**, *323*, 109–121.

(35) Restani, R.; Martin, M.; Kivel, N.; Gavillet, D. *J. Nucl. Mater.* **2009**, *385*, 435–442.

(36) Degueldre, C.; Pouchon, M.; Döbeli, M.; Sickafus, K.; Hojou, K.; Ledergerber, G.; Abolhassani-Dadras, S. *J. Nucl. Mater.* **2001**, *289*, 115–121.

(37) Keyes, R. W. *Phys. Rev.* **1959**, *115*, 564–567.

(38) Angeles-Rosas, M.; Camacho-López, M. A.; Ruiz-Trejo, E. *Solid State Ionics* **2010**, *181*, 1349–1354.

(39) Haering, C.; Roosen, a; Schichl, H.; Schnoller, M. *Solid State Ionics* **2005**, *176*, 261–268.

(40) Yamamoto, O.; Arati, Y.; Takeda, Y.; Imanishi, N.; Mizutani, Y.; Kawai, M.; Nakamura, Y. *Solid State Ionics* **1995**, *79*, 137–142.

(41) Seaborg, G. T. *Radiochim. Acta* **1993**, *61*, 115–122.

(42) Villarreal, R.; Spall, D. *Selection of Actinide Chemical Analogues for WIPP Tests*; Los Alamos, 1995.

(43) Shannon, R. D. *Acta Crystallogr., Sect. A Found. Crystallogr.* **1976**, *32*, 751–767.

(44) Arachi, Y. *Solid State Ionics* **2004**, *175*, 119–121.

(45) PANalytical HighScore Plus Version 3.0.4 (2011) PANaltyical BV: Amelo, The Netherlands.

(46) Igawa, N.; Ishii, Y. *J. Am. Ceram. Soc.* **2001**, *84*, 1169–1171.

(47) Bondars, B.; Heidemane, G.; Grabis, J.; Laschke, K.; Boysen, H.; Schneider, J.; Frey, F. *J. Mater. Sci.* **1995**, *30*, 1621–1625.

(48) Jaffe, J.; Bachorz, R.; Gutowski, M. *Phys. Rev. B* **2005**, *72*, 144107.

(49) Heald, S. M.; Brewe, D. L.; Stern, E. A.; Kim, K. H.; Brown, F. C.; Jiang, D. T.; Crozier, E. D.; Gordon, R. A. *J. Synchrotron Rad.* **1999**, *6*, 347–349.

(50) Thompson, A.; Attwood, D.; Gullikson, E.; Howells, M.; Kim, K.-J.; Kirz, J.; Kortright, J.; Lindau, I.; Pianetta, P.; Robinson, A.; Scofield, J.; Underwood, J.; Vaughn, D.; Williams, G.; Winick, H. *X-ray Data Booklet*; Lawrence Berkeley National Laboratory: Berkeley, 2009.

(51) Ravel, B.; Newville, M. *J. Synchrotron Rad.* **2005**, *12*, 537–541.

(52) Newville, M. *Fundamentals of XAFS*, 1.7 ed.; University of Chicago: Chicago, 2004.

(53) Hayes, J. R.; Grosvenor, A. P.; Saoudi, M. *J. Alloys Compd.* **2015**, *635*, 245–255.

(54) Rehr, J.; Albers, R. *Phys. Rev. B* **1990**, *41*, 8139–8149.

(55) Hu, Y. F.; Coulthard, I.; Chevrier, D.; Wright, G.; Igarashi, R.; Sitnikov, A. *AIP Conf. Proc.* **2010**, *1234*, 343–346.

(56) Pecharsky, V. K.; Zavalij, P. Y. *Fundamentals of Powder Diffraction and Structural Characterization of Materials*, 2nd ed.; Springer US: Boston, MA, 2009.

(57) Fujimori, H.; Yashima, M.; Kakihana, M.; Yoshimura, M. *J. Appl. Phys.* **2002**, *91*, 6493–6498.

(58) Sakuma, T.; Suto, H. *J. Mater. Sci.* **1986**, *21*, 4359–4365.

(59) Fujimori, H.; Yashima, M.; Kakihana, M.; Yoshimura, M. *J. Am. Ceram. Soc.* **1998**, *81*, 2885–2893.

(60) Zhang, J.; Wang, Y. Q.; Valdez, J. a.; Tang, M.; Won, J.; Sickafus, K. E. *Nucl. Instruments Methods Phys. Res. Sect. B Beam Interact. with Mater. Atoms* **2012**, *272*, 244–248.

(61) Denton, A.; Ashcroft, N. *Phys. Rev. A* **1991**, *43*, 3161–3164.

(62) Mountjoy, G.; Holland, M. A.; Wallidge, G. W.; Gunawidjaja, P.; Smith, M. E.; Pickup, D. M.; Newport, R. J. *J. Phys. Chem. B* **2003**, *107*, 7557–7566.

(63) Mountjoy, G.; Pickup, D. M.; Anderson, R.; Wallidge, G. W.; Holland, M. A.; Newport, R. J.; Smith, M. E. *Phys. Chem. Chem. Phys.* **2000**, *2*, 2455–2460.

(64) Li, P.; Chen, I.-W.; Penner-Hahn, J. E. *Phys. Rev. B* **1993**, *48*, 10074–10081.

(65) Kim, N.; Hsieh, C.; Stebbins, J. F. *Chem. Mater.* **2006**, *18*, 3855–3859.

(66) Bogicevic, a.; Wolverton, C. *Phys. Rev. B* **2003**, *67*, 024106.

(67) Oberti, R.; Quartieri, S.; Dalconi, M. C.; Boscherini, F.; Iezzi, G.; Boiocchi, M.; Eeckhout, S. G. *Am. Mineral.* **2006**, *91*, 1230–1239.

(68) Lindqvist-Reis, P.; Persson, I.; Sandström, M. *Dalton Trans.* **2006**, *32*, 3868–3878.

(69) Li, P.; Chen, I.-W.; Penner-Hahn, J. E.; Tien, T.-Y. *J. Am. Ceram. Soc.* **1991**, *74*, 958–967.

(70) Yamamoto, T. *X-Ray Spectrom.* **2008**, *37*, 572–584.

(71) Aluri, E. R.; Grosvenor, A. P. *J. Alloys Compd.* **2014**, *616*, 516–526.

(72) Aluri, E. R.; Grosvenor, A. P. *Phys. Chem. Chem. Phys.* **2013**, *15*, 10477–10486.

(73) Wu, Z.; Benfatto, M.; Natoli, C. *Phys. Rev. B* **1998**, *57*, 10336–10339.

(74) Allred, A. L. *J. Inorg. Nucl. Chem.* **1961**, *17*, 215–221.

(75) Omar, S.; Bonanos, N. *J. Mater. Sci.* **2010**, *45*, 6406–6410.

(76) Yamamura, H.; Matsusita, T.; Nishino, H.; Kakinuma, K. *J. Mater. Sci. Mater. Electron.* **2002**, *13*, 57–61.

(77) Yamamura, H. *Solid State Ionics* **1998**, *107*, 185–189.

## Tables

### Table 1 Parameters of powder XRD Rietveld Refinement

| | **$Nd_{0.25}Zr_{0.75}O_{1.88}$** | | | **$Nd_{0.20}Sc_{0.05}Zr_{0.75}O_{1.88}$** | | |
|---|---|---|---|---|---|---|
| | **As synth** | **An. 1100 °C** | **An. 1400 °C** | **As synth** | **An. 1100 °C** | **An. 1400 °C** |
| Rwp | 8.08 | 8.51 | 8.85 | 10.33 | 11.74 | 12.94 |
| Unit Cell | 5.1791(3) | 5.2156(5) | 5.2079(1) | 5.1614(1) | 5.1658(5) | 5.1565(1) |
| Wt. Fraction | 100% Cubic | 64.7% Cubic<br>35.3% Tetragonal | 65.7% Cubic<br>3.5% Tetragonal<br>30.9% Monoclinic | 100% Cubic | 67.4% Cubic, 32.6% Tetragonal | 91.2% Cubic<br>8.8% Monoclinic |
| | **$Nd_{0.15}Sc_{0.10}Zr_{0.75}O_{1.88}$** | | | **$Nd_{0.10}Sc_{0.15}Zr_{0.75}O_{1.88}$** | | |
| Rwp | **As synth** | **An. 1100 °C** | **An. 1400 °C** | **As synth** | **An. 1100 °C** | **An. 1400 °C** |
| Unit Cell | 6.38 | 12.07 | 12.50 | 8.21 | 8.70 | 13.48 |
| Wt. Fraction | 5.1252(5) | 5.1303(3) | 5.1321(1) | 5.1080(6) | 5.1121(2) | 5.1128(1) |
| | 100% Cubic | 100% Cubic | 100% Cubic | 100% Cubic | 100% Cubic | 100% Cubic |
| | **$Nd_{0.05}Sc_{0.20}Zr_{0.75}O_{1.88}$** | | | **$Sc_{0.25}Zr_{0.75}O_{1.88}$** | | |
| | **As synth** | **An. 1100 °C** | **An. 1400 °C** | **As synth** | **An. 1400 °C** | |
| Rwp | 7.89 | 9.41 | 11.24 | 7.90 | 10.86 | |
| Unit Cell | 5.0885(5) | 5.0921(1) | 5.09130(8) | 5.0828(3) | 5.0857(3) | |
| Wt. Fraction | 100% Cubic | 100% Cubic | 100% Cubic | 100% Cubic | 30.8% Cubic<br>69.2% β-Phase | |

### Table 2 Zr K-edge EXAFS Fitting Results

$Sc_{0.25}Zr_{0.75}O_{1.88}$

| | As-synthesized $S_o^2 = 0.98(7)$, $\Delta E = -1.7(8)$ eV $R_{fit} = 0.017$ | | | Annealed 1400 °C $S_o^2 = 1.00(8)$ $\Delta E = -3(1)$ eV $R_{fit} = 0.020$ | | |
|---|---|---|---|---|---|---|
| | CN | R (Å) | $\sigma^2$ | CN | R (Å) | $\sigma^2$ |
| Zr–O | 7 | 2.149(8) | 0.008(1) | 7 | 2.152(9) | 0.008(1) |
| Zr–Zr | 9 | 3.55(1) | 0.012(1) | 9 | 3.53(1) | 0.011(2) |
| Zr–Sc | 3 | 3.57(5) | 0.017(8) | 3 | 3.56(5) | 0.015(8) |
| Zr–O2 | 24 | 4.26(4) | 0.05(1) | 24 | 4.21(8) | 0.05(1 |

$Nd_{0.15}Sc_{0.10}Zr_{0.75}O_{1.88}$

| | As-synthesized $S_o^2 = 0.93(9)$ $\Delta E = -2.8(9)$ eV $R_{fit} = 0.014$ | | | Annealed 1400 °C $S_o^2 = 0.94(7)$ $\Delta E = -1.7(7)$ eV $R_{fit} = 0.014$ | | |
|---|---|---|---|---|---|---|
| | CN | R (Å) | $\sigma^2$ | CN | R (Å) | $\sigma^2$ |
| Zr–O | 7 | 2.160(8) | 0.008(1) | 7 | 2.158(8) | 0.008(1) |
| Zr–Zr | 9 | 3.57(2) | 0.012(2) | 9 | 3.58(2) | 0.012(2) |
| Zr–Sc | 2 | 3.58(4) | 0.005(6) | 1.8 | 3.53(4) | 0.006(6) |
| Zr–Nd | 1 | 3.61(3) | 0.004(3) | 1.2 | 3.36(3) | 0.004(2) |
| Zr–O2 | 22 | 4.29(4) | 0.03(1) | 22 | 4.30(5) | 0.029(8) |

**Figure Captions**

**Figure 1** Powder XRD patterns from the as-synthesized and annealed ternary (a) $Nd_{0.25}Zr_{0.75}O_{1.88}$ and (b) $Sc_{0.25}Zr_{0.75}O_{1.88}$ materials are presented. In all figures "As-synth." indicates as-synthesized material and "An." indicates an annealed sample. Peaks from monoclinic (1) and tetragonal (2) $ZrO_2$ phases form when the $Nd_{0.25}Zr_{0.75}O_{1.88}$ material was annealed at 1400 °C. Peaks associated with a β-phase Sc-Zr-O material, marked with an asterisk, were observed when the $Sc_{0.25}Zr_{0.75}O_{1.88}$ material was annealed at 1400 °C. There is good agreement between the data and the fits generated by Rietveld analysis in all cases.

**Figure 2** The powder X-ray diffraction patterns from the quaternary as-synthesized and annealed (a) $Nd_{0.05}Sc_{0.20}Zr_{0.75}O_{1.88}$ and (b) $Nd_{0.20}Sc_{0.05}Zr_{0.75}O_{1.88}$ materials are presented. A small monoclinic impurity phases formed when the $Nd_{0.20}Sc_{0.05}Zr_{0.75}O_{1.88}$ material was annealed at 1400 °C while the $Nd_{0.05}Sc_{0.20}Zr_{0.75}O_{1.88}$ remained a single-phase upon annealing. There is good agreement between the data and the fits generated by Rietveld analysis in all cases.

**Figure 3** SE images from pellets of the as synthesized (a) $Nd_{0.25}Zr_{0.75}O_{1.88}$, (b) $Nd_{0.20}Sc_{0.05}Zr_{0.75}O_{1.88}$, (c) $Nd_{0.05}Sc_{0.20}Zr_{0.75}O_{1.88}$, and (d) $Sc_{0.25}Zr_{0.75}O_{1.88}$ materials and the (e) $Nd_{0.25}Zr_{0.75}O_{1.88}$, (f) $Nd_{0.20}Sc_{0.05}Zr_{0.75}O_{1.88}$, (g) $Nd_{0.05}Sc_{0.20}Zr_{0.75}O_{1.88}$, and (h) $Sc_{0.25}Zr_{0.75}O_{1.88}$ pellets annealed at 1400 °C. Upon annealing the pellet surface flattens and more surface pores are visible.

**Figure 4** Nd $L_\alpha$ EDS maps from the as-synthesized (a) $Nd_{0.25}Zr_{0.75}O_{1.88}$, (b) $Nd_{0.20}Sc_{0.05}Zr_{0.75}O_{1.88}$, (c) $Nd_{0.05}Sc_{0.20}Zr_{0.75}O_{1.88}$ pellets and the (d) $Nd_{0.25}Zr_{0.75}O_{1.88}$, (e) $Nd_{0.20}Sc_{0.05}Zr_{0.75}O_{1.88}$ and (f) $Nd_{0.05}Sc_{0.20}Zr_{0.75}O_{1.88}$ pellets annealed at 1400 °C. The Nd became segregated when the pellet was annealed at high temperature.

**Figure 5** Sc $K_\alpha$ EDS maps from the as-synthesized (a) $Nd_{0.20}Sc_{0.05}Zr_{0.75}O_{1.88}$, (b) $Nd_{0.05}Sc_{0.20}Zr_{0.75}O_{1.88}$, and (c) $Sc_{0.25}Zr_{0.75}O_{1.88}$ materials and the (d) $Nd_{0.20}Sc_{0.05}Zr_{0.75}O_{1.88}$, (e) $Nd_{0.05}Sc_{0.20}Zr_{0.75}O_{1.88}$, and (f) $Sc_{0.25}Zr_{0.75}O_{1.88}$ materials annealed at 1400 °C.) No change in the Sc distribution was observed when the pellets were annealed at 1400 °C.

**Figure 6** Zr $K_\alpha$ EDS maps from pellets of the as synthesized (a) $Nd_{0.25}Zr_{0.75}O_{1.88}$, (b) $Nd_{0.20}Sc_{0.05}Zr_{0.75}O_{1.88}$, (c) $Nd_{0.05}Sc_{0.20}Zr_{0.75}O_{1.88}$, and (d) $Sc_{0.25}Zr_{0.75}O_{1.88}$ materials and the (e) $Nd_{0.25}Zr_{0.75}O_{1.88}$, (f) $Nd_{0.20}Sc_{0.05}Zr_{0.75}O_{1.88}$, (g) $Nd_{0.05}Sc_{0.20}Zr_{0.75}O_{1.88}$, and (h) $Sc_{0.25}Zr_{0.75}O_{1.88}$ pellets annealed at 1400 °C. The Zr was homogenously distributed in all of the as-synthesized and annealed samples.

**Figure 7** (a) Zr K-edge XANES spectra from the as-synthesized $Nd_xSc_yZr_{1-x-y}O_{2-\delta}$ materials are presented. Three features, labelled A, B and C are observed. Feature A arises from forbidden, quadrupolar Zr 1s → 4d transitions while features B and C are due to dipolar Zr 1s → 5p transitions. (b) The spectra from the as-synthesized materials are compared to the spectra from the materials annealed at 1400 °C. Only the spectrum from the $Nd_{0.25}Zr_{0.75}O_{1.88}$ materials changes upon annealing.

**Figure 8** (a) Zr K-edge EXAFS spectra from several of the as-synthesized $Nd_xSc_yZr_{1-x-y}O_{2-\delta}$ materials are presented. Three features, labelled D, E, and E' are observed: feature D arises from Zr–O scattering paths and features E is attributed to the Zr–Zr, Zr–Sc, and Zr–Nd scattering paths. The contributions to feature E' are mostly attributable to the Zr–Sc scattering path. (b) The Zr EXAFS spectra from the as-synthesized and annealed $Nd_{0.15}Sc_{0.10}Zr_{0.75}O_{1.88}$ materials are compared. There is little change in the intensity of Feature D while the intensity of Features E and E' increase as the annealing temperature increases. (c) The fits of the Zr K-edge spectra are compared to the data in R-space and (d) k-space.

**Figure 9** (a) The Zr $L_3$-edge XANES spectra from several of the as-synthesized $Nd_xSc_yZr_{1-x-y}O_{2-\delta}$ materials. Two features, F and G, were observed. Feature F is assigned to Zr 2p → 3d $e_g$ excitations and feature G is assigned to Zr 2p → 3d $t_{2g}$ states. The intensity of Feature G increases as the Sc content increases. (b) The Zr $L_3$-edge XANES spectra from several of the as-synthesized and annealed materials are compared. Changes are observed when several of the materials are annealed, but no trend is observed.

**Figure 10** (a) Sc K-edge XANES spectra from several of the as-synthesized $Nd_xSc_yZr_{1-x-y}O_{2-\delta}$ materials. Features $H_1$, $H_2$, and $H_3$ arise from forbidden Sc 1s → 3d transitions and Features $I_1$ and $I_2$ are attributed to dipole-allowed Sc 1s → 4p transitions. There is a decrease in the intensity of Feature $I_1$ and an increase in the intensity of Feature $I_2$ as the Sc content decreases. (b) The Sc K-edge XANES spectra from several of the as-synthesized and annealed materials are compared. The intensity of feature $I_2$ increases as the annealing temperature increases. The magnitude of the change in the spectra observed upon annealing increases with increasing Sc content.

**Figure 11** (a) Nd $L_3$-edge spectra from the as-synthesized $Nd_xSc_yZr_{1-x-y}O_{2-\delta}$ compounds. A strong white line is observed and the magnitude of this line increases with as the Sc content increased. (b) The Nd $L_3$-edge spectra from the as-synthesized and annealed materials are compared. No significant changes were observed upon annealing.

**Figures**

Figure 1

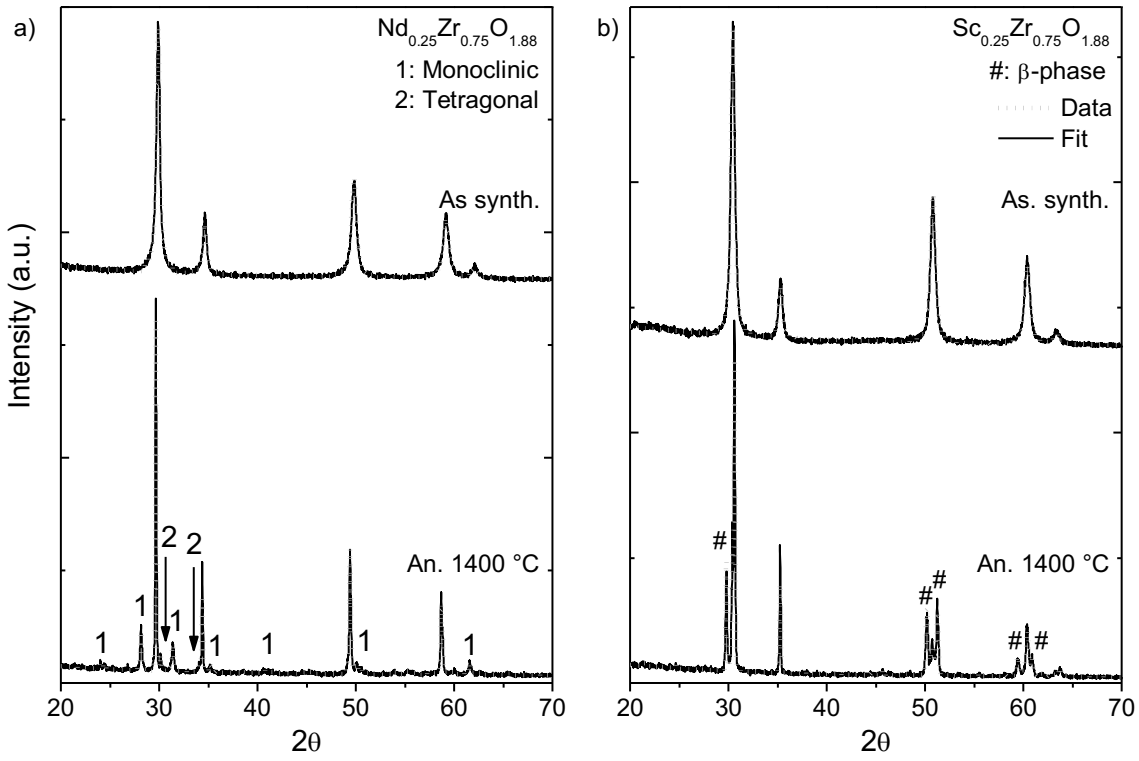

Figure 2

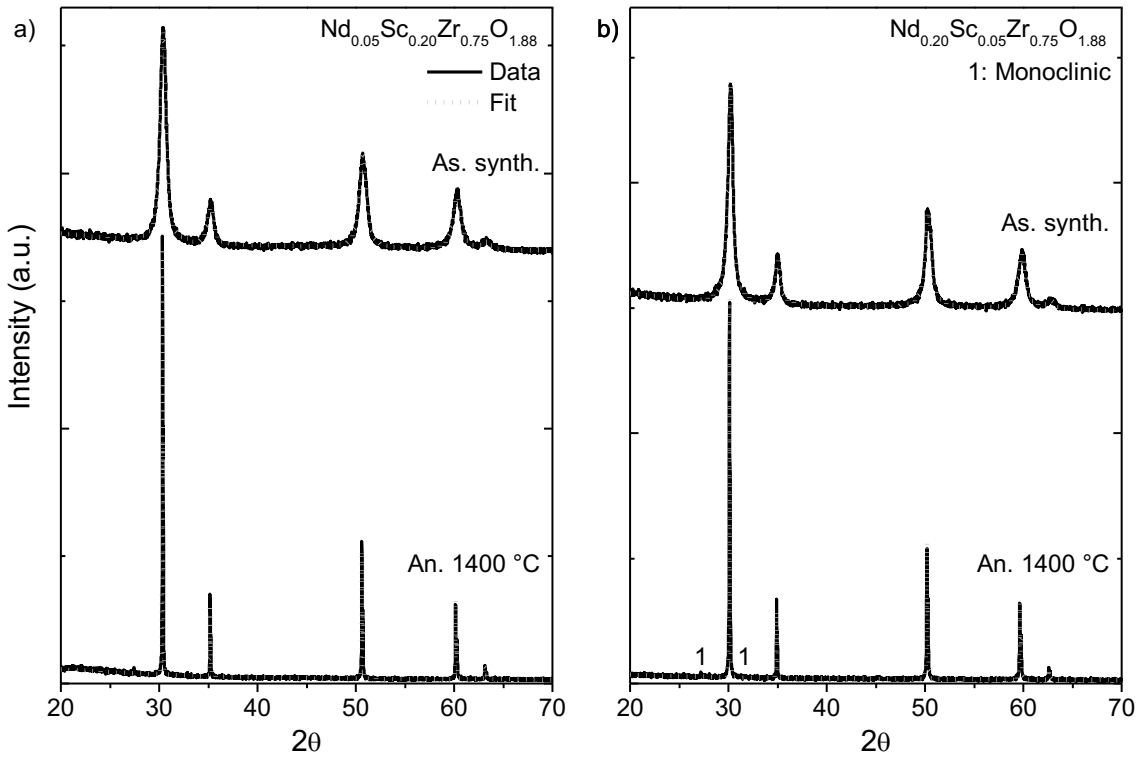
a)
$Nd_{0.05}Sc_{0.20}Zr_{0.75}O_{1.88}$
Data
Fit
As. synth.
An. 1400 °C
Intensity (a.u.)
20
30
40
50
60
70
2θ
b)
$Nd_{0.20}Sc_{0.05}Zr_{0.75}O_{1.88}$
1: Monoclinic
As. synth.
An. 1400 °C
1
1
20
30
40
50
60
70
2θ

Figure 3

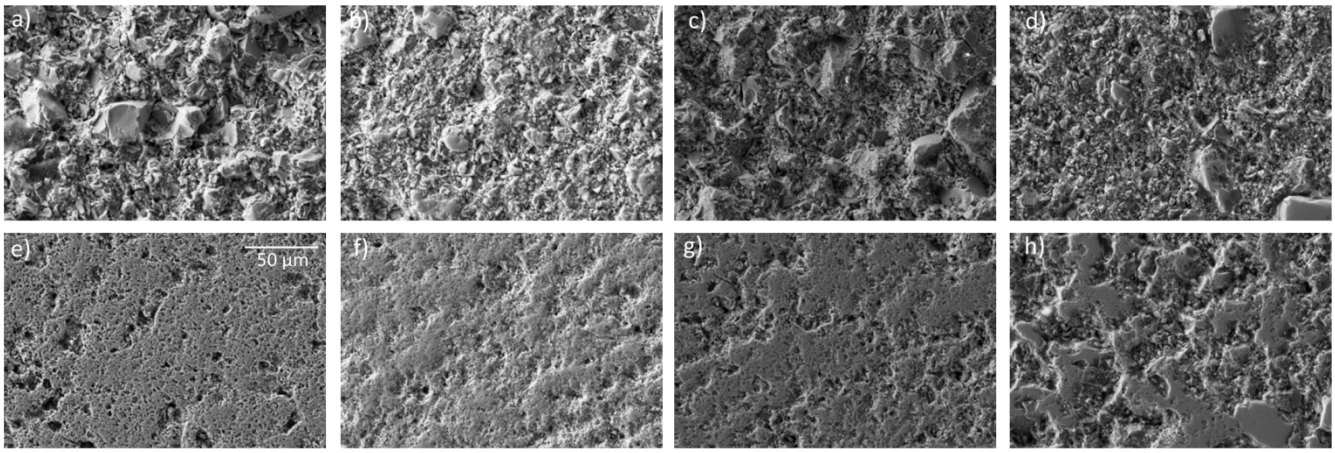

Figure 4

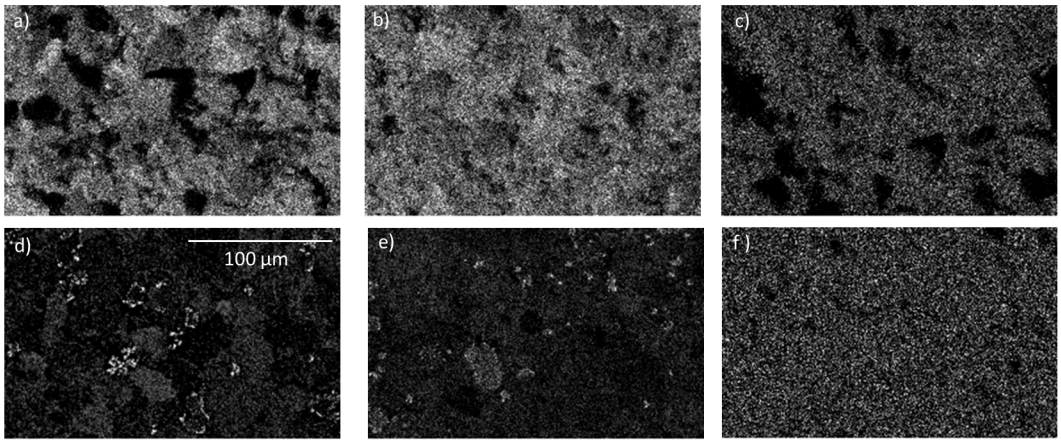

Figure 5

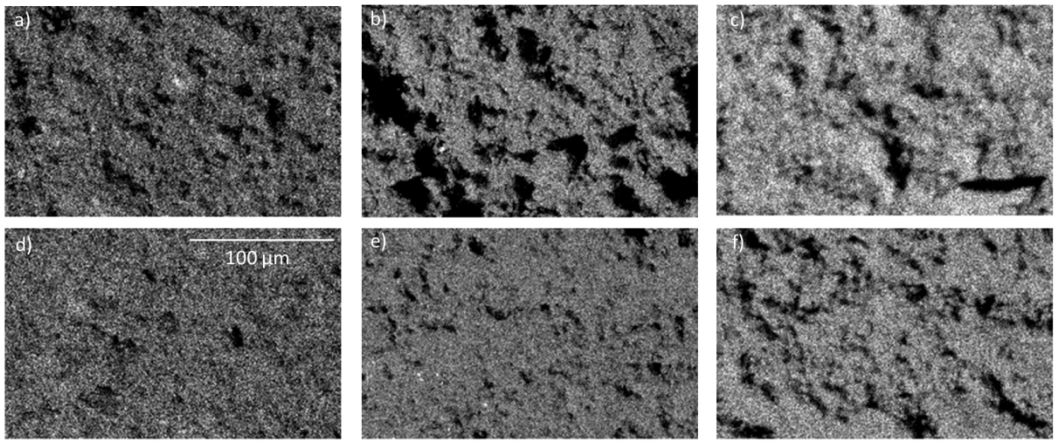

Figure 6

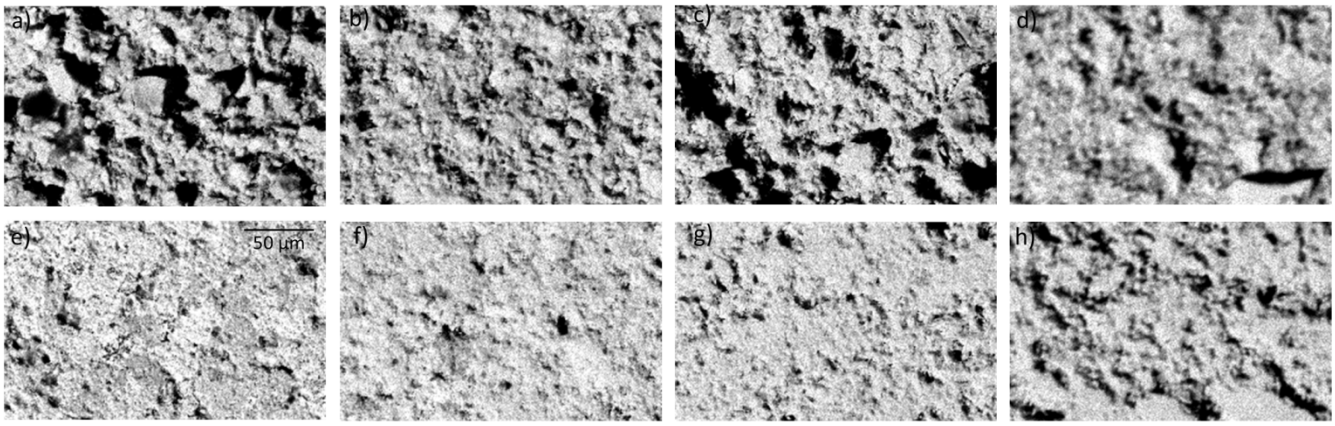

Figure 7

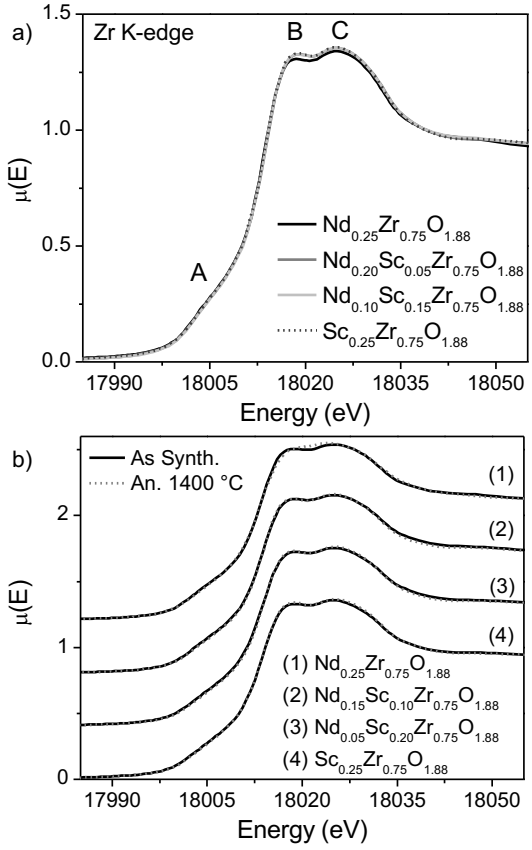
a)
Zr K-edge
A
B
C
μ(E)
Energy (eV)
Nd0.25Zr0.75O1.88
Nd0.20Sc0.05Zr0.75O1.88
Nd0.10Sc0.15Zr0.75O1.88
Sc0.25Zr0.75O1.88
b)
As Synth.
An. 1400 °C
(1)
(2)
(3)
(4)
(1) Nd0.25Zr0.75O1.88
(2) Nd0.15Sc0.10Zr0.75O1.88
(3) Nd0.05Sc0.20Zr0.75O1.88
(4) Sc0.25Zr0.75O1.88

Figure 8

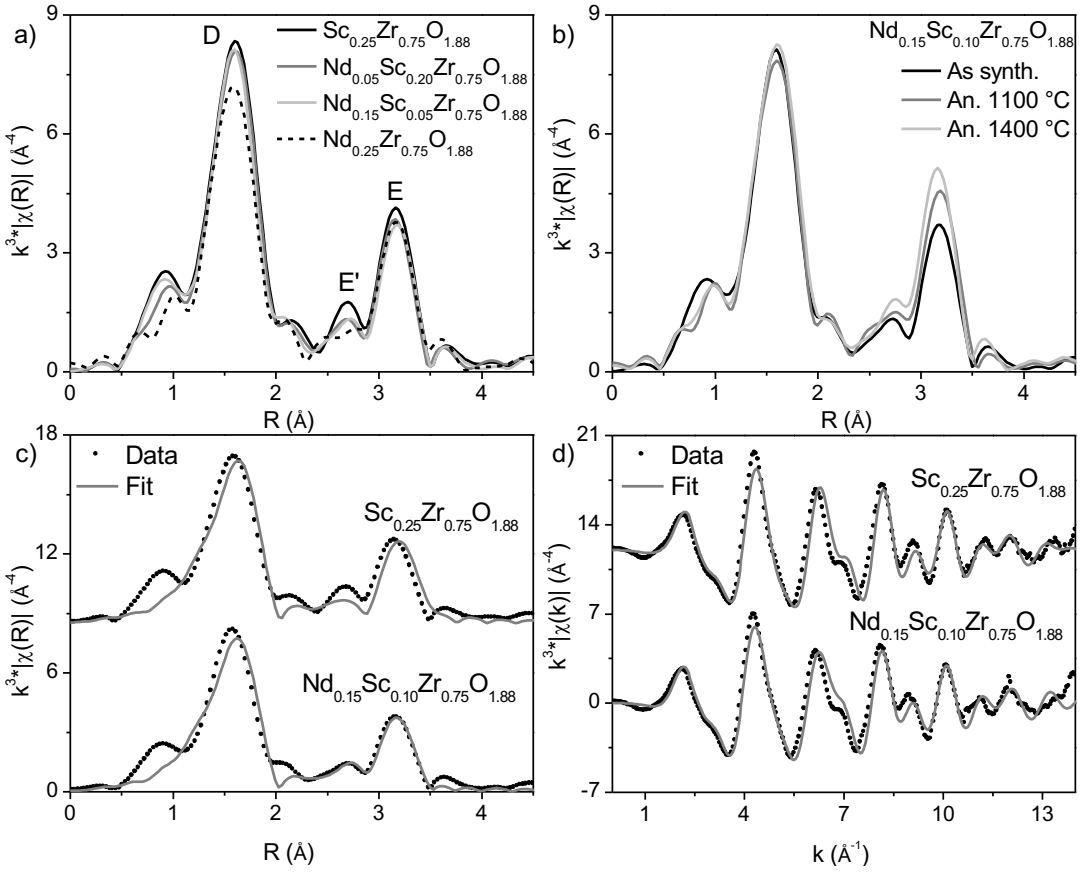
a)
D
E
E'
$Sc_{0.25}Zr_{0.75}O_{1.88}$
$Nd_{0.05}Sc_{0.20}Zr_{0.75}O_{1.88}$
$Nd_{0.15}Sc_{0.05}Zr_{0.75}O_{1.88}$
$Nd_{0.25}Zr_{0.75}O_{1.88}$
$k^3*|\chi(R)|$ (Å$^{-4}$)
R (Å)
b)
$Nd_{0.15}Sc_{0.10}Zr_{0.75}O_{1.88}$
As synth.
An. 1100 °C
An. 1400 °C
$k^3*|\chi(R)|$ (Å$^{-4}$)
R (Å)
c)
Data
Fit
$Sc_{0.25}Zr_{0.75}O_{1.88}$
$Nd_{0.15}Sc_{0.10}Zr_{0.75}O_{1.88}$
$k^3*|\chi(R)|$ (Å$^{-4}$)
R (Å)
d)
Data
Fit
$Sc_{0.25}Zr_{0.75}O_{1.88}$
$Nd_{0.15}Sc_{0.10}Zr_{0.75}O_{1.88}$
$k^3*|\chi(k)|$ (Å$^{-4}$)
k (Å$^{-1}$)

Figure 9

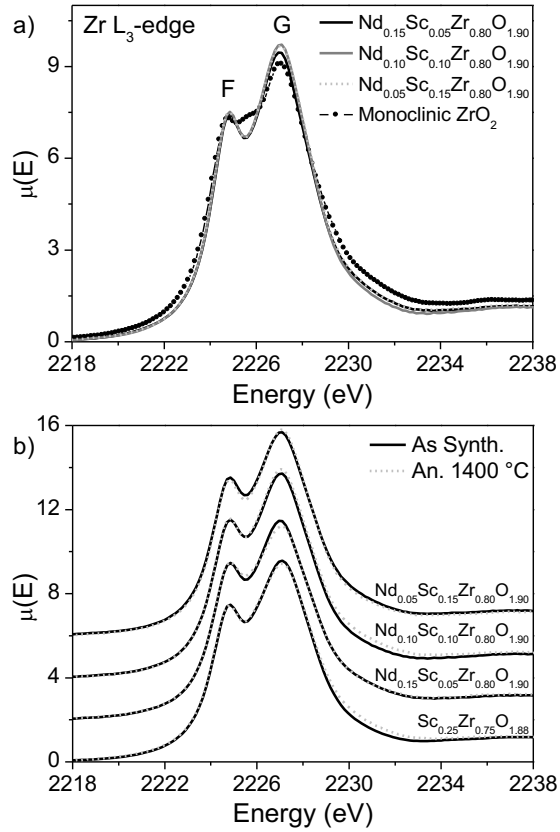
a)
Zr L3-edge
F
G
Nd0.15Sc0.05Zr0.80O1.90
Nd0.10Sc0.10Zr0.80O1.90
Nd0.05Sc0.15Zr0.80O1.90
Monoclinic ZrO2
μ(E)
Energy (eV)
b)
As Synth.
An. 1400 °C
Nd0.05Sc0.15Zr0.80O1.90
Nd0.10Sc0.10Zr0.80O1.90
Nd0.15Sc0.05Zr0.80O1.90
Sc0.25Zr0.75O1.88
μ(E)
Energy (eV)

Figure 10

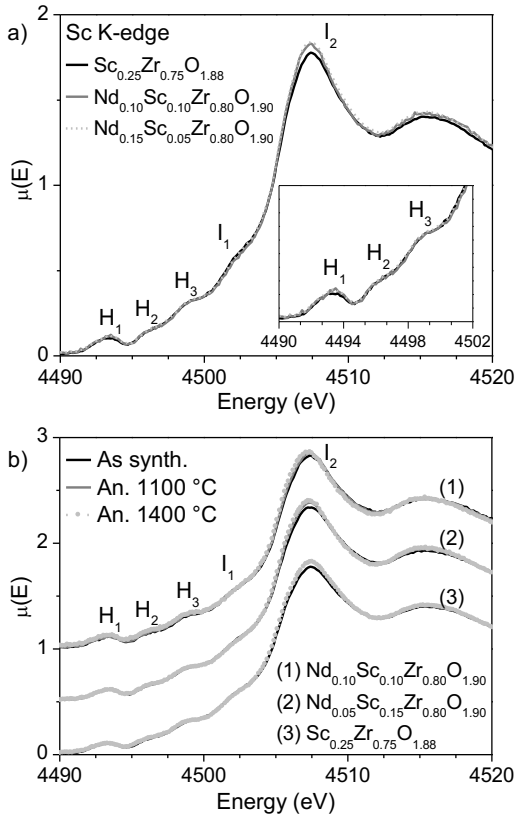
a)
Sc K-edge
Sc0.25Zr0.75O1.88
Nd0.10Sc0.10Zr0.80O1.90
Nd0.15Sc0.05Zr0.80O1.90
I2
I1
H3
H2
H1
μ(E)
Energy (eV)
b)
As synth.
An. 1100 °C
An. 1400 °C
(1)
(2)
(3)
(1) Nd0.10Sc0.10Zr0.80O1.90
(2) Nd0.05Sc0.15Zr0.80O1.90
(3) Sc0.25Zr0.75O1.88

Figure 11

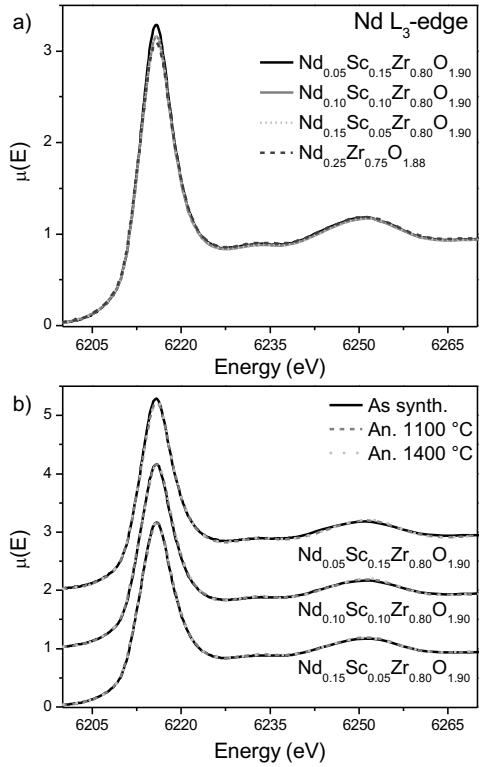
a)
Nd L3-edge
Nd0.05Sc0.15Zr0.80O1.90
Nd0.10Sc0.10Zr0.80O1.90
Nd0.15Sc0.05Zr0.80O1.90
Nd0.25Zr0.75O1.88
μ(E)
Energy (eV)
b)
As synth.
An. 1100 °C
An. 1400 °C
Nd0.05Sc0.15Zr0.80O1.90
Nd0.10Sc0.10Zr0.80O1.90
Nd0.15Sc0.05Zr0.80O1.90
μ(E)
Energy (eV)

**For Table of Contents Only:**

The thermal stability of possible cubic $Nd_xSc_yZr_{1-x-y}O_{2-\delta}$ inert matrix fuels has been studied by annealing the materials at 1100 °C and 1400 °C. (Nd was used as a surrogate for Am.) The long-range and local structures of the materials were studied using powder X-ray diffraction, scanning electron microscopy, and X-ray absorption spectroscopy. The results show the cubic fluorite structure was only stable at high temperatures when $x+y > 0.15$ and $y \geq 0.10$.